Electron–hole asymmetry of the topological surface states in strained HgTe

Andreas Jost[a,b], Michel Bendias[c], Jan Böttcher[d], Ewelina Hankiewicz[d], Christoph Brüne[c], Hartmut Buhmann[c], Laurens W. Molenkamp[c], Jan C. Maan[a,b], Uli Zeitler[a,b], Nigel Hussey[a,b], and Steffen Wiedmann[a,b,1]

[a]High Field Magnet Laboratory–European Magnetic Field Laboratory, Radboud University, 6525 ED Nijmegen, The Netherlands; [b]Institute for Molecules and Materials, Radboud University, 6525 ED Nijmegen, The Netherlands; [c]Physikalisches Institut, Universität Würzburg, 97074 Wuerzburg, Germany; and [d]Institut für Theoretische Physik und Astrophysik, Universität Würzburg, 97074 Wuerzburg, Germany

Edited by Subir Sachdev, Harvard University, Cambridge, MA, and approved February 6, 2017 (received for review July 15, 2016)

Topological insulators are a new class of materials with an insulating bulk and topologically protected metallic surface states. Although it is widely assumed that these surface states display a Dirac-type dispersion that is symmetric above and below the Dirac point, this exact equivalence across the Fermi level has yet to be established experimentally. Here, we present a detailed transport study of the 3D topological insulator-strained HgTe that strongly challenges this prevailing viewpoint. First, we establish the existence of exclusively surface-dominated transport via the observation of an ambipolar surface quantum Hall effect and quantum oscillations in the Seebeck and Nernst effect. Second, we show that, whereas the thermopower is diffusion driven for surface electrons, both diffusion and phonon drag contributions are essential for the hole surface carriers. This distinct behavior in the thermoelectric response is explained by a strong deviation from the linear dispersion relation for the surface states, with a much flatter dispersion for holes compared with electrons. These findings show that the metallic surface states in topological insulators can exhibit both strong electron–hole asymmetry and a strong deviation from a linear dispersion but remain topologically protected.

topological insulators | surface states | thermopower | quantum Hall effect

Topological insulators (TIs) possess metallic surface states that display a Dirac-type dispersion relation, whereas they are insulating in the bulk (1–4). Despite enormous experimental effort in recent years, access to the topological surface states (TSSs) and the ability to distinguish them from bulk contributions in transport experiments remain a significant challenge. The investigation of their transport properties in the bismuth-chalcogenides compounds, for example, has been hindered by excessive electron doping, which shifts the Fermi energy into the bulk conduction band (5, 6). This energy shift can be circumvented by adding additional hole doping to bring the Fermi energy back into the band gap, and indeed, a surface quantum Hall effect (SQHE) has been observed in nearly stoichiometric $BiSbTeSe_2$ (7).

The predicted linear dispersion of TSSs on 3D TIs is reminiscent of graphene, the prototype 2D Dirac material. Magnetothermoelectric transport experiments on graphene have shown that S_{xx} as a function of the applied gate voltage V_g is in quantitative agreement with the semiclassical Mott formula (8–10) (i.e., thermopower is symmetric and diffusion-driven for electrons and holes), and no signatures of phonon drag have been observed, implying that electron–phonon coupling is weak in graphene (11). Although bismuth-chalcogenides are widely investigated thermoelectric materials for refrigeration and power dependence at room temperature (12), only a few studies to date address the thermopower of TSS, for example, on Bi_2Se_3 (13) and $(Bi_{1-x}Sb_x)Te_3$ (14). In Bi_2Se_3, the gate-dependent zero-field thermoelectric power is found to be in agreement with the Mott relation near the charge neutrality point at low temperatures (13). Quantum oscillations in S_{xx} have been observed in Bi_2Te_3, but their interpretation has been hindered by the presence of a significant bulk contribution (15).

In contrast to bismuth-chalcogenide compounds, where both bulk and surface states are present, strained HgTe is the material of choice to investigate transport properties that are unique to the TSS. Strained HgTe is another 3D TI with a relatively small band gap, which is naturally undoped, and can be grown with a very high quality, exceeding the mobility of comparable Bi-based systems by more than one order of magnitude (16–18). This extreme purity coupled with the absence of any notable bulk conductance lead to a quantum Hall (QH) response that is dominated by the Dirac-like surface states (17). The presence of TSS is unambiguously shown here by the observation of ambipolar SQHE. Moreover, we explore in detail the nature of the TSSs in strained HgTe through low-temperature measurements of resistance and Seebeck and Nernst effect in a high magnetic field B on either side of the Dirac point. At $B = 0$, we show that thermopower is dominantly diffusion-driven for surface electrons in agreement with the results on Bi_2Se_3 (13) and graphene (8–10). In contrast, thermopower for surface holes shows a significant phonon drag contribution. Accompanying band-structure calculations reveal the origin of this electron–hole asymmetry in the thermoelectric response.

Results and Discussion

Ambipolar SQHE. In Fig. 1 *A*–*C*, we illustrate the observation of the ambipolar SQHE accompanied by Shubnikov–de Haas

Significance

Topological insulators possess metallic surfaces states that are generally perceived as electrons and holes with a linear symmetric dispersion around the Dirac point. In this work, we show that this symmetry is significantly distorted in the 3D topological insulator-strained HgTe. In thermopower experiments, we show a distinctively different behavior of surface electrons and holes that originates from a strongly asymmetric dispersion of surface states. Nonetheless, the surface states themselves remain topologically protected as evidenced by the observation of an ambipolar surface quantum Hall effect and quantum oscillations in the thermoelectric response. This observation shows that the physics of topological surface states in 3D topological insulators is far richer than previously envisaged.

Author contributions: A.J., C.B., H.B., L.W.M., and S.W. designed research; A.J., M.B., C.B., J.C.M., U.Z., N.H., and S.W. performed research; A.J., J.B., E.H., and S.W. analyzed data; M.B. prepared the samples; J.B. and E.H. performed theoretical band-structure calculations; and A.J. and S.W. wrote the paper with input from all coauthors.

The authors declare no conflict of interest.

This article is a PNAS Direct Submission.

[1]To whom correspondence should be addressed. Email: s.wiedmann@science.ru.nl.

This article contains supporting information online at www.pnas.org/lookup/suppl/doi:10.1073/pnas.1611663114/-/DCSupplemental.

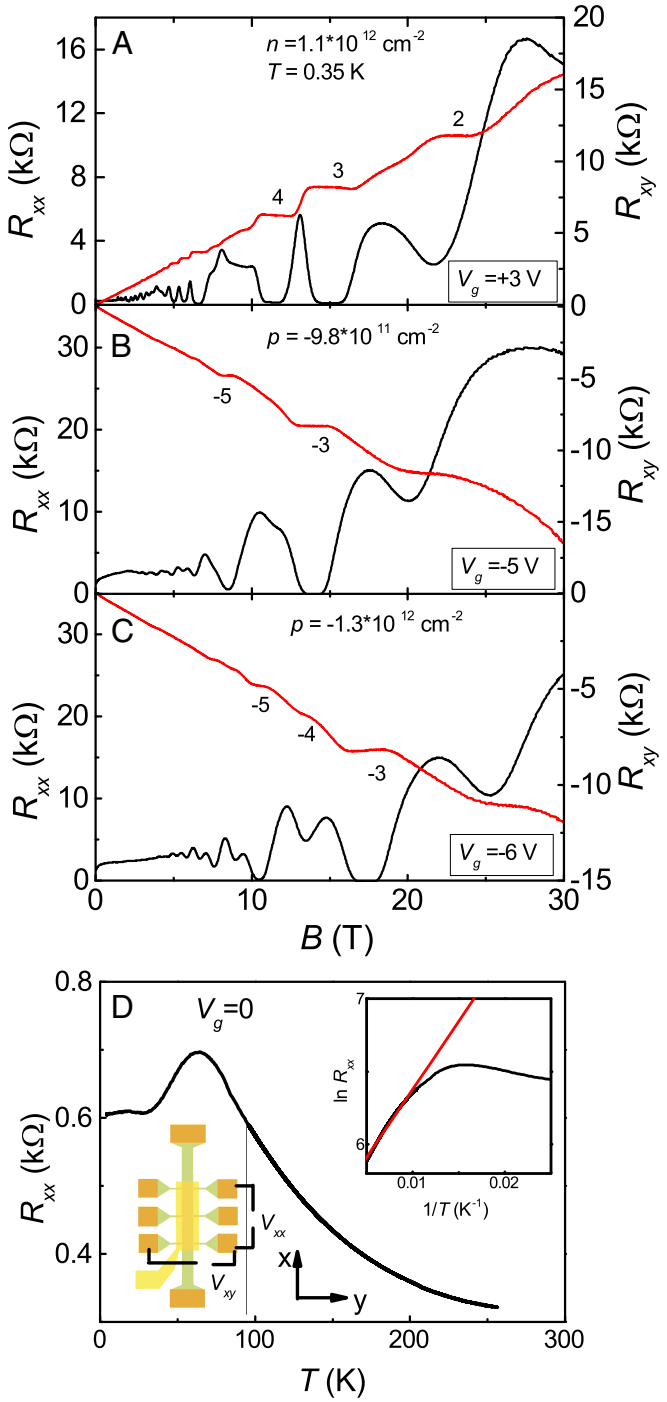

Fig. 1. Electrical transport and ambipolar SQHE in strained HgTe. (*A–C*) Quantum oscillations in R_{xx} (black lines) and SQHE in R_{xy} (red lines) for different charge-carrier concentrations (several integer filling factors are labeled) at T = 0.35 K. In B, the hole charge-carrier concentrations of both surfaces are approximately equal. (*D*) R_{xx} as a function of T at a gate voltage $V_g = 0$ V. The metallic TSSs dominate transport for $T < 65$ K. (*Inset*) Extraction of the thermal activation gap lnR_{xx} (1/T) of 16 meV (red line) and sample layout with the Hall bar in light green and gate and contacts in gold. *B*, magnetic field; R_{xx}, longitudinal resistance; R_{xy}, Hall resistance; T, temperature; T, tesla; V_g, gate voltage.

oscillations in the resistance R_{xx} at different V_g. We use a top gate to tune the charge-carrier concentration n from the electron region ($n \simeq 1.4 \cdot 10^{12}$ cm^{-2}) through the charge neutrality point deep into the hole regime ($p \simeq -1.3 \cdot 10^{12}$ cm^{-2}). The observation of ambipolar SQHE is definitive evidence for 2D transport that originates in 3D TIs exclusively from the surface states. The total charge-carrier concentration extracted from the slope of the low-field Hall resistance, n_{Hall}, depends linearly on the gate voltage (*SI Text*). From the zero-field resistivity and n_{Hall}, we extract a carrier mobility at 0.35 K from $1.5{\cdot}10^5$ to $3.0{\cdot}10^5$ cm^2/Vs for electrons and from $2.0{\cdot}10^4$ to $9.0{\cdot}10^4$ cm^2/Vs for holes.

Because of the Dirac nature of charge carriers, TSSs exhibit the half-integer QH effect, where the Hall conductivity is quantized as $\sigma_{xy}^{\mathrm{t(b)}} = \nu_{\mathrm{t(b)}} e^2/h$ with $\nu_{\mathrm{t(b)}} = (N_{\mathrm{t(b)}} + 1/2)$ as the filling factor for each surface and $N_{\mathrm{t(b)}}$ as the Landau-level index of the top (bottom) surface. The quantized Hall conductivity is accompanied by a zero conductivity $\sigma_{xx} = 0$. Therefore, the total Hall resistance is $R_{xy} = 1/\sigma_{xy}^{\mathrm{t(b)}} = h/(N_{\mathrm{t}} + N_{\mathrm{b}} + 1)e^2$ (7, 16–18). In general, when the charge-carrier concentrations of the top and bottom surfaces are different, both odd and even integer QH plateaus appear with zeros in R_{xx} (Fig. 1 *A*, electrons and *C*, holes). When the charge-carrier concentrations of the surfaces are approximately equal, however, only odd integer QH plateaus [i.e., $R_{xy} = h/(2N+1)e^2$] are observed (Fig. 1*B*) because of the existence of two degenerate Dirac systems. A more comprehensive transport analysis on another sample is presented in *SI Text* and illustrated in Fig. S3.

The dominance of the metallic surface states in the low-temperature resistance is further exemplified in Fig. 1*D*, where we show the temperature dependence of R_{xx} at $V_g = 0$. With decreasing temperature, R_{xx} increases strongly down to ∼65 K because of thermally activated bulk carriers (the Arrhenius plot in Fig. 1*D*, *Inset* gives an activation gap of $\Delta \simeq 16$ meV) that are still dominant. For $T < 65$ K, R_{xx} becomes dominated by the metallic surface states apparent in a decrease of the resistance that saturates at low temperatures.

Thermoelectric Coefficients. Having established unambiguously the dominance of TSS in the magnetotransport, we now turn to investigate the thermoelectric response of our films. Thermopower, also referred to as the Seebeck effect S_{xx}, is the voltage that arises when a thermal gradient is applied along the sample. This voltage is needed to compensate for the thermally driven electron current, and thus, it does not depend directly on the scattering time τ but does depend on the derivative of τ with respect to the energy $d\tau/d\varepsilon \propto d\sigma/d\varepsilon$ at the Fermi level, where σ is the conductivity (19). Thus, thermopower compared with other transport properties, such as conductivity, is more sensitive to details of the band structure. In metallic systems, thermopower originates predominantly from two different mechanisms: diffusion and phonon drag. The former arises from the nonequilibrium of the Fermi–Dirac distribution of the electrons caused by a thermal gradient. In the latter, phonons travel down the heat gradient, displacing charge carriers in their wake. Independent of the mechanism, S_{xx} is almost exclusively negative for electrons and positive for holes (19). In a 3D TI, extra care needs to be taken to disentangle contributions from both surface- and bulk-derived states.

We first focus on the low-field electrical and thermal transport as a function of gate voltage as presented in Fig. 2. The longitudinal resistance R_{xx} as a function of V_g (Fig. 2*A*) has a pronounced maximum at $V_g \simeq -1.35$ V, whereas the Hall resistance R_{xy} crosses 0 at $V_g = -1.85$ V (vertical dashed line in Fig. 2*A*) for B = 0.2 T. For higher (lower) V_g, R_{xy} is positive (negative) pointing toward dominant electron (hole) charge carriers. We, therefore, assign the 0 crossing of R_{xy} at $V_g = -1.85$ V to the charge neutrality point of the surface states. At this point, R_{xx} is ≃85% of its value at the maximum.

The thermopower S_{xx} as a function of V_g at $B = 0$ is shown in Fig. 2*B*. A change in sign in S_{xx} is observed at $V_g = -0.3$ V, corresponding to a transition from dominant electron to dominant

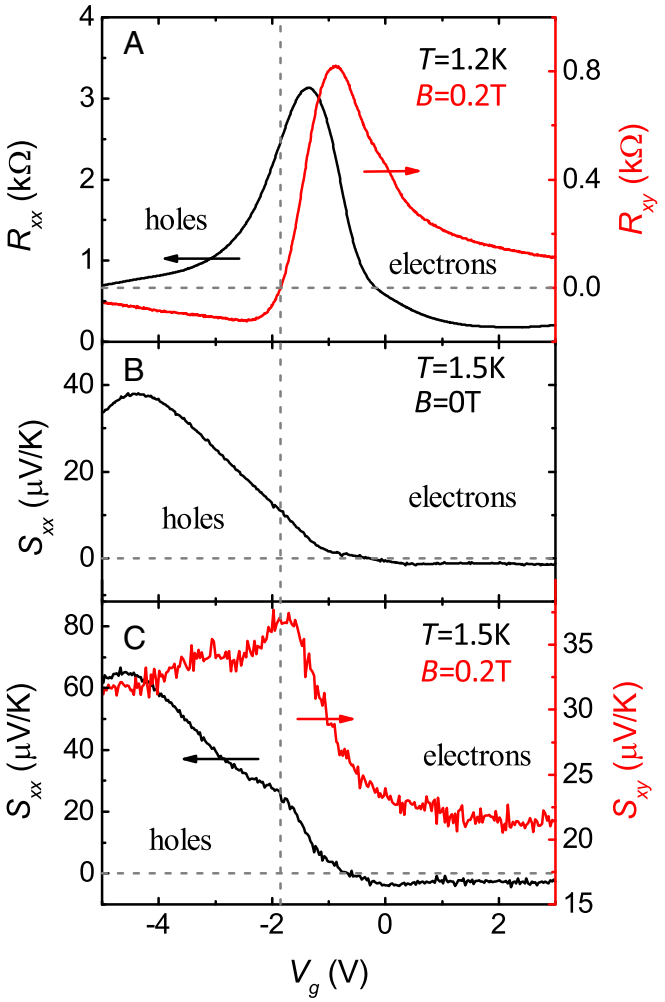

Fig. 2. Low-field electrical and thermal transport of strained HgTe at 1.2 and 1.5 K, respectively. (*A*) Gate voltage dependence of the resistance R_{xx} and Hall resistance at B = 0.2 T. The position of the Dirac point where R_{xy} crosses zero is marked by a vertical dashed line. (*B*) Gate voltage dependence of the thermoelectric power S_{xx} at B = 0 T. (*C*) Gate voltage dependence of the thermopower S_{xx} and Nernst effect S_{xy} at 0.2 T: a small hump in S_{xx} is observed, where a gap opens at the Dirac point (vertical line). B, magnetic field; R_{xx}, longitudinal resistance; R_{xy}, Hall resistance; S_{xx}, thermopower; S_{xy}, Nernst coefficient; T, temperature; V_g, gate voltage.

hole contributions. At positive gate voltages, S_{xx} is negative—as expected for electrons—and constant over a wide range of gate voltages. Its magnitude is surprisingly small, however, with a value of only a few microvolts per kelvin, comparable with that seen in correlated high-density metals (20, 21). The zero crossing in S_{xx} occurs at a more positive value of V_g than the zero crossing of R_{xy}. Below $V_g = -1.0$ V, S_{xx} starts to increase strongly up to a maximum of 37 μV/K at $V_g = -4.4$ V. This observation raises an important question: why is the thermopower for holes so much larger than that for electrons?

To quantify the diffusion thermopower S_d for electrons and holes, we use the Mott formula, which is given by

$$S_d = \frac{\pi^2}{3}\frac{k_B^2 T}{q}\frac{1}{\sigma}\frac{d\sigma}{d\varepsilon}\bigg|_{\varepsilon_F} = \frac{\pi^2}{3}\frac{k_B^2 T}{q}\frac{1}{\sigma}\frac{d\sigma}{dn}D(V_g) \qquad [1]$$

with k_B as the Boltzmann constant, q as the electron/hole charge, n as the charge-carrier concentration, and $D(V_g)$ as the density of states at a certain gate voltage measured from the Dirac point (13). Although the conductivity σ and $d\sigma/dn$ can be extracted directly from our measurements, to obtain $D(V_g)$, we need the effective mass of surface carriers, which can be obtained independently (e.g., from band-structure calculations as shown below).

Band-Structure Calculations. Band-structure calculations were performed based on the six-band $k \cdot p$ approach (22) for a heterostructure comprised of $Cd_{0.7}Hg_{0.3}Te/HgTe/Cd_{0.7}Hg_{0.3}Te$. We use an effective Hartree potential in the spirit of the Dirac screening model as introduced for electron surface states in ref. 16. To account for the large range of carrier concentration observed, we primarily dope the Dirac surface state from the n- to the p-type carrier concentrations for a large range of gate voltages, whereas the structure of the bulk bands is weakly affected. This phenomenological approach is motivated by the disagreement between self-consistent Hartree calculations (23) and our magnetotransport results in the regime of the SQHE accompanied by $R_{xx} = 0$ as well as the fact that we are able to tune the charge-carrier concentration on the top and bottom surfaces by the top gate. More details on transport are presented in *SI Text*. In contrast to the approach in ref. 16, we consider an additional interface potential arising from a reduced point symmetry (24), which introduces a coupling between the light-hole (LH) and heavy-hole (HH) components, even at $k = 0$. The interface potential is adjusted such that the position of the Dirac point in the $k \cdot p$ model coincides approximately with ab initio calculations (25) and angular-resolved photo-emission spectroscopy results (16, 26), where it was found that, for ungated HgTe, the Dirac point is located several tens of millielectronvolts below the HH band edge.

The dispersion relations $E(k)$ are shown in Fig. 3 for $V_g = 1$ V and $V_g = -3$ V. $V_g = 1$ V corresponds to a large electron density, where the densities on the top and bottom surfaces differ. As a result, odd and even plateaus are observed in the Hall resistance as shown in Fig. 1*A*. $V_g = -3$ V corresponds to a small hole density, with the densities on the top and bottom surfaces being approximately the same in this case. These equal densities give rise to only odd plateaus in the Hall resistance R_{xy}, similar to those observed in Fig. 1*B*. In the dispersion relation in Fig. 3, we clearly identify the TSSs. Remarkably, the chemical potential μ remains in the bulk band gap throughout the whole range of carrier concentrations in agreement with the experimental observation of SQHE, even for large hole carrier concentrations (Fig. 1*C*). One of the most striking features of the band dispersions of the TSS, however, is the strong departure from a strictly linear (Dirac-like) behavior caused by the strong coupling of the TSS with the HH subbands. Such a deviation from strict linearity was observed first in angular-resolved photoemission experiments on Bi_2Se_3 (27). Using our combined techniques, we are able to address the intrinsic charge-carrier properties across the Fermi level by tuning the top gate voltage V_g. From the dispersion relations in HgTe (Fig. 3), we obtain an effective mass of $m_e \approx 0.02\, m_0$ for surface electrons at $V_g = 1$ V and $m_h \approx 0.11\, m_0$ at $V_g = -3$ V for surface holes, where m_0 is the free electron mass. The thermopower is now calculated at $V_g = 1$ V to be $S_d \simeq -0.7$μV/K, which is in excellent agreement with the experimental data, suggesting that thermopower for surface electrons is purely diffusion-driven. For holes, however, we estimate the diffusion contribution to be $S_d \simeq 2$μV/K, more than one order of magnitude smaller than the experimental value at $V_g = -3$ V.

Phonon Drag Thermopower. To gain more insight into the mechanisms governing S_{xx}, we investigate its temperature dependence at different gate voltages as shown in Fig. 4. At lower temperatures, the thermopower for electrons is small and independent on V_g, with a weak linear temperature dependence consistent with a pure diffusion-driven mechanism (Fig. 4, *Inset*). In contrast, S_{xx}

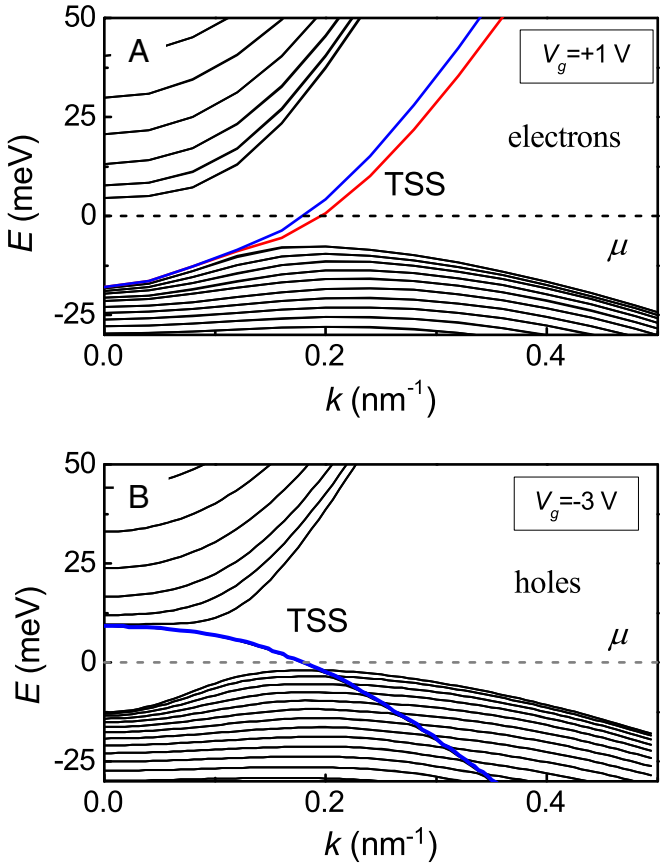

Fig. 3. Band-structure calculations based on the six-band $k \cdot p$ approach (bulk bands are in black, and TSSs are in red and blue). $E(k)$ for (*A*) electrons at $V_g = 1$ V and (*B*) holes at $V_g = -3$ V when the TSSs are degenerate. The dashed lines represent the chemical potential μ. *E*, energy; meV, milli electron volt; V_g, gate voltage.

for holes is much larger in absolute magnitude over a wide range of temperatures and exhibits a peak at around $T = 12$ K. Phonon drag thermopower is known to give rise to large signals (28), with a maximum when the phonon heat conductivity is largest (28), which is at 7 K for CdTe (substrate) (29) and 13 K for HgTe (30). This correspondence implies that the enhanced thermopower in the hole-dominated region indeed originates from a significant phonon drag contribution that intriguingly is absent on the electron side. The origin of this dichotomy is, we believe, in the heavier mass of the hole carriers that is reflected in the flatter band dispersion (31). The sharp drop in S_{xx} suggests that, at elevated temperatures, electrons are also excited to the bulk conduction band and begin to dominate the zero-field thermopower.

In the presence of a small magnetic field of $B = 0.2$ T (Fig. 2*C*), S_{xx} shows the same overall behavior as at $B = 0$ but develops a small hump at $V_g = -1.85$ V directly at the Dirac point (vertical dashed line in Fig. 2) that likely originates from a gapping of surface states at the Dirac point when a magnetic field is applied. The Nernst effect S_{xy} (i.e., the voltage perpendicular to the heat gradient) is a very sensitive probe of charge carriers in solids. S_{xy} is small in systems with a single type of charge carriers but large when electrons and holes coexist or in the presence of high-mobility charge carriers (32). In strained HgTe, S_{xy} is found to have a maximum at $V_g = -1.85$ V exactly at the zero crossing of R_{xy}. The low-field Nernst effect for electrons is small at positive gate voltages (Fig. 2*C*). On the hole side, S_{xy} decreases with increasing V_g but remains large compared with the electron side as found in S_{xx}. We note that, in gated samples, not only the parts of the sample underneath the gate but also, the n-doped legs of the Hall bar contribute to S_{xy} (Fig. S2). This contribution of the legs gives rise to a constant offset in the measurement when sweeping the gate voltage that does not invalidate our conclusion (*SI Text*).

Seebeck and Nernst Effect in a Quantizing Magnetic Field. In Fig. 5 *A* and *B*, thermopower and resistivity are plotted as a function of the magnetic field up to $B = 16$ T at $T = 1.5$ K at fixed charge-carrier concentrations for electrons ($V_g = +3.0$ V) and holes ($V_g = -4.5$ V). Pronounced quantum oscillations originating from both surface electrons and holes are observed.

The oscillations in thermopower mimic those in electrical resistivity (Fig. 5 *A* and *B*). Because thermopower is proportional to the derivative of the conductivity with respect to the energy (33), the oscillations are shifted by $\pi/2$. On the electron side (Fig. 5*A*), the minima are very deep and even reach zero at higher fields. Likewise, on the hole side (Fig. 5*B*), clear quantum oscillations are observed. At $V_g = -4.5$ V, we only observe oscillations in S_{xx} that correspond to odd filling factors as expected for two degenerate Dirac systems with equal carrier concentrations. With decreasing gate voltage, even filling factors appear as the charge-carrier concentrations of the two surfaces become different (Fig. 5*C*). Therefore, the observed sequence of quantum oscillations in S_{xx} as a function of B independently confirms the presence of two surfaces on a 3D TI.

Next, we focus on the oscillatory behavior of S_{xx} as a function of the magnetic field. When the magnetic field is increased, the chemical potential sweeps through the Landau levels, and S_{xx} has a maximum for half-filled levels. Diffusion thermopower is a direct measure of the entropy of electrons per unit charge density, and at low temperatures, it has been shown that, in the disorder free limit, the amplitudes of the quantum oscillations

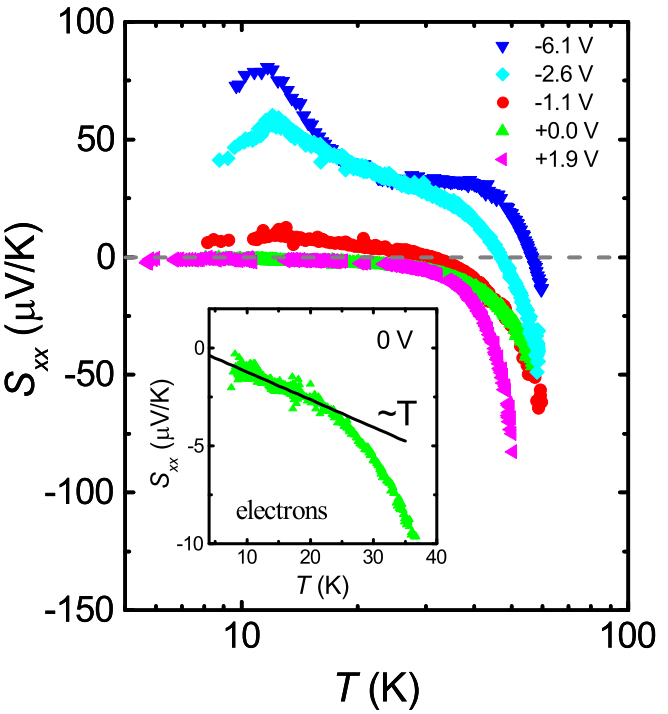

Fig. 4. Temperature dependence of the thermopower S_{xx} at different charge-carrier concentrations (gate voltage V_g). The thermopower is small and nearly flat for electrons ($V_g = 0$ and 1.9 V) and large for holes with a phonon drag peak visible at 12 K at $V_g = -2.6$ and -6.1 V. *Inset* highlights the linear dependence of S_{xx} as a function of temperature for electrons for $V_g = 0$. S_{xx}, thermopower; *T*, temperature; T, tesla.

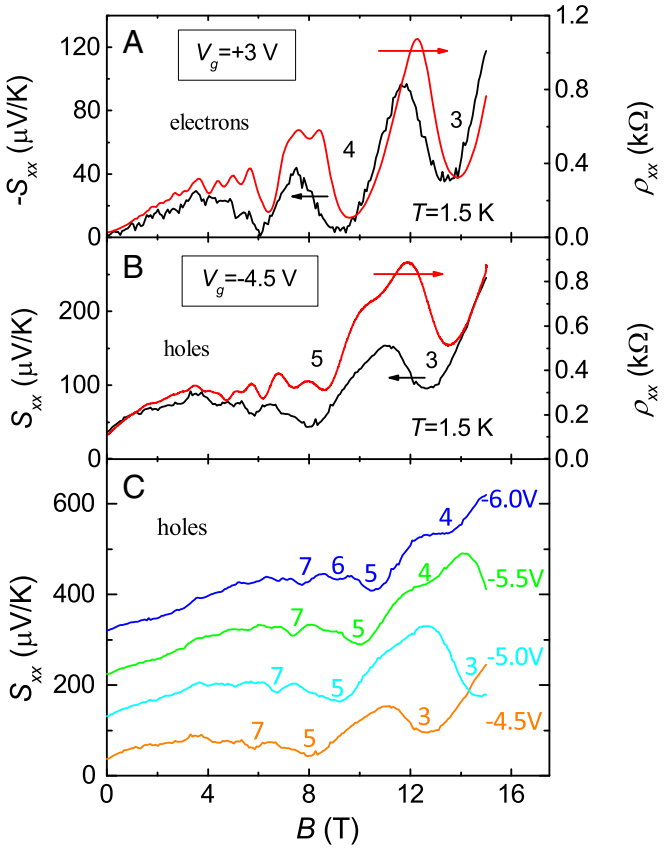

Fig. 5. Quantum oscillations in thermopower and resistivity at T = 1.5 K as a function of the magnetic field at different carrier concentrations. S_{xx} and R_{xx} at (*A*) V_g = +3.0 V (electrons) and (*B*) V_g = −4.5 V (holes). The oscillations in thermopower are shifted by $\pi/2$ with respect to the resistance. (*C*) The thermopower for holes at different carrier concentrations as a function of B shows the evolution from the odd integer filling factors (V_g = −4.5 V) at equal carrier concentrations on either surface to odd and even filling factors (V_g = −6.0 V). *B*, magnetic field; S_{xx}, thermopower; *T*, temperature; T, tesla; V_g, gate voltage; ρ_{xx}, resistivity.

have universal values that depend only on their index $N(\simeq 40\mu/\mathrm{K}$ for $N=1)$ (34). For our system, we observe that the amplitude of the quantum oscillations of the TSS is considerably larger than the expected universal values for diffusion thermopower for both electrons and holes. Our observation is in agreement with conventional 2D systems, such as GaAs heterojunctions, and suggests that the phonon drag contribution plays an essential role in a magnetic field (35, 36).

Finally, to highlight the coexistence of electron and hole carriers, we have measured the Nernst effect S_{xy} and thermopower S_{xx} along with electrical transport in a moderate magnetic field of 9 T as a function of V_g as illustrated in Fig. 6. Pronounced quantum oscillations are observed in R_{xx}, thermopower S_{xx}, and the Nernst effect S_{xy} for both electrons and holes accompanied by the SQHE in R_{xy}, which shows clear plateaus at several integer filling factors. We find the zero crossing of R_{xy} (charge neutrality) and the maximum in S_{xy} at $V_g = -1$ V. The zero crossing in S_{xx} corresponding to the transition from electrons to holes occurs at a slightly higher V_g, which was found for the maximum in R_{xx}.

In conclusion, we have presented ambipolar electrical and thermal transport properties in high-quality 3D TI-strained HgTe in a wide range of carrier concentrations. We find that the thermoelectric response is purely diffusion-driven for surface electrons, whereas for surface holes, it is dominated by a large phonon drag contribution. This marked asymmetry in the thermoelectric response makes the TSSs in strained HgTe distinct from other Dirac systems, such as graphene. In high magnetic fields, we have observed pronounced quantum oscillations for both surface electrons and holes accompanied by the SQHE. In band-structure calculations, we have confirmed the absence of any bulk transport in our system and shown that the asymmetry of the thermoelectric response derives from a corresponding asymmetry in the dispersion of the surface states. Despite the significant departure from a simple linear dispersion, the surface states remain topologically protected. This observation shows that the physics of TSS in 3D TIs is far richer than previously envisaged.

Materials and Methods

Samples Σ1 and Σ2 (*SI Text* and Fig. S1) are two different pieces of the same HgTe wafer with a thickness of 104 nm grown on a CdTe (001) substrate by molecular beam epitaxy. Sample Σ3 is a 60-nm HgTe layer that is sandwiched between two $Hg_{0.3}Cd_{0.7}Te$ buffer layers on top (5 nm) and bottom (100 nm), and it is also presented in *SI Text*. CdTe has a slightly larger lattice constant than HgTe, inducing strain on the sample. The strain opens an energy gap of $E_g \simeq 22$ meV between the Γ_8 LH and the Γ_8 HH bands, turning strained HgTe into a 3D TI. For samples thicker than ∼150 nm (37), the strain relaxes by dislocations. Sample Σ4, shown in *SI Text*, has a thickness of 600 nm and is, therefore, a 3D semimetal (see data in Fig. S4). All samples are patterned in Hall bar geometry with a mesa of 1.2-mm length and 200-μm width using argon etching. A schematic of the sample is shown

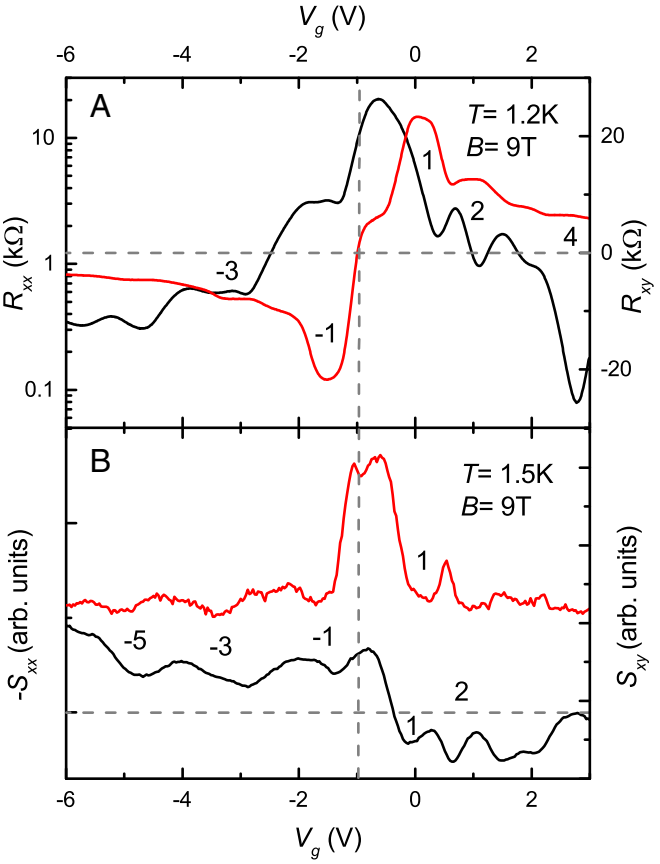

Fig. 6. Magnetotransport and thermopower at $B = 9$ T as a function of V_g. (*A*) R_{xx} and R_{xy} exhibit quantum oscillations and a quantized Hall resistance for both electrons and holes. (*B*) S_{xx} and the Nernst effect S_{xy} also show clear quantum oscillations. The maximum in S_{xy} corresponds to the zero crossing of R_{xy}. The numbers are the integer filling factors. arb, arbitrary; *B*, magnetic field; R_{xx}, longitudinal resistance; R_{xy}, Hall resistance; S_{xx}, thermopower; S_{xy}, Nernst coefficient; *T*, temperature; V_g, gate voltage.

PHYSICS

in Fig. 1*D*, *Inset*. Care was taken to ensure that the legs running to the contact pads are perpendicular to the applied heat gradient to avoid additional contributions to longitudinal thermoelectric voltage by the legs. Samples $\Sigma 1$, $\Sigma 2$, and $\Sigma 3$ are equipped with a 100-nm-thick Au top gate covering the middle of the sample and parts of the legs separated from the HgTe bulk material by a 110-nm-thick multilayer insulator of SiO_2/Si_3N_4.

For the thermopower measurements, the sample was mounted free standing in a vacuum chamber and glued with one end to a silver stripe, which was connected to an He bath (cold sink). An electric heater was attached to the other end of the sample to apply a heat gradient, which was monitored by two matched 3-kΩ ruthenium oxide thermometers glued to the backside of the sample. To ensure that the sample is not thermally shorted by the gate, the heat gradient was cross-checked using the two-point resistance between the upper and lower legs as thermometers. The thermoelectric power has been measured by applying a very low-frequency ($\sim$ 0.03 Hz) square wave-shaped current to the heater, and the thermoelectromotive force ΔV was recorded by nanovoltmeters.

The measurements of longitudinal and transverse electrical resistances were conducted in a four-point geometry with low constant voltage excitation to avoid self-heating. Throughout the paper, all values are given as resistance instead of units of resistivity in either 2D or 3D. To obtain the resistivity, all values have to be multiplied by the factor $1/6$ for the 2D resistivity or $1/6 \cdot 10^{-7}$ m for the 3D resistivity. Samples $\Sigma 1$ and $\Sigma 2$ were mounted in a ^{4}He system with a base temperature of 1.2 K in a 16-T superconducting magnet. For the temperature dependence, sample $\Sigma 1$ was mounted in a Variable Temperature Insert. Sample $\Sigma 3$ was investigated in a ^{3}He system at a base temperature of 0.3 K, whereas sample $\Sigma 4$ was measured in a ^{4}He flow cryostat with a base temperature of 1.2 K in a 37.5-T Bitter magnet.

ACKNOWLEDGMENTS. We thank Benoît Fauqué for fruitful discussions. This work was performed at the High Field Magnet Laboratory Radboud University/Fundamental Research on Matter, member of the European Magnetic Field Laboratory and supported by EuroMagNET II under European Union (EU) Contract 228043. The group from Universität Würzburg acknowledges funding from the German Research Foundation (The Leibniz Program, Sonderforschungsbereich 1170 "Tocotronics," and Schwerpunktprogramm 1666), EU European Research Council Advanced Grant Program Project 3-TOP, and the Elitenetzwerk Bayern Internationales Dokoranden Kolleg "Topologische Isolatoren." This work was supported by German Science Foundation Grant HA 5893/4-1 within Schwerpunkt Program 1666 (to J.B. and E.H.); J.B. and E.H. thank the Elite Bayern Network Graduate School "Topological insulators" for financial support. Financial support was provided by Nederlandse Organisatie voor Wetenschappelijk Onderzoek VENI Grant 680-47-424 (to S.W.).

1. Hasan MZ, Kane CL (2010) Colloquium: Topological insulators. *Rev Mod Phys* 82:3045–3067.
2. Qi X-L, Zhang S-C (2011) Topological insulators and superconductors. *Rev Mod Phys* 83:1057–1110.
3. Ando Y (2013) Topological insulator materials. *J Phys Soc Jpn* 82:102001.
4. Hsieh D, et al. (2009) A tunable topological insulator in the spin helical Dirac transport regime. *Nature* 460:1101–1106.
5. Analytis JG, et al. (2010) Two-dimensional surface state in the quantum limit of a topological insulator. *Nat Phys* 6(12):960–964.
6. Qu DX, Hor YS, Xiong J, Cava RJ, Ong NP (2010) Quantum oscillations and hall anomaly of surface states in the topological insulator Bi_2Te_3. *Science* 329:821–824.
7. Xu Y, et al. (2014) Observation of topological surface state quantum Hall effect in an intrinsic three - dimensional topological insulator. *Nat Phys* 10:956–963.
8. Zuev YM, Chang W, Kim P (2009) Thermoelectric and magneto-thermoelectric transport measurements of graphene. *Phys Rev Lett* 102:096807.
9. Wei P, Bao W, Pu Y, Lau CN, Shi J (2009) Anomalous thermoelectric transport of Dirac particles in graphene. *Phys Rev Lett* 80:166808.
10. Checkelsky JG, Ong NP (2009) Thermopower and Nernst effect in graphene in a magnetic field. *Phys Rev B* 80:081413(R).
11. Hwang EH, Rossi E, das Sarma S (2009) Theory of thermopower in two-dimensional graphene. *Phys Rev B* 80:235415.
12. Goldsmid HJ (2014) Bismuth telluride and its alloys as materials for thermodynamic generation. *Materials (Basel)* 7(4):2577–2592.
13. Kim D, Syers P, Butch NP, Paglione J, Fuhrer MS (2014) Ambipolar surface state thermoelectric power of topological insulator Bi_2Se_3. *Nano Lett* 14(4):1701–1706.
14. Zhang J, et al. (2015) Disentangling the magnetoelectric and thermoelectric transport in topological insulator thin films. *Phys Rev B* 91:075431.
15. Qu DX, Hor YS, Cava RJ (2012) Quantum oscillations in magnetothermopower measurements of the topological insulator Bi_2Te_3. *Phys Rev Lett* 109:246602.
16. Brüne C, et al. (2011) Quantum Hall effect from the topological surface states of strained bulk HgTe. *Phys Rev Lett* 106:126803.
17. Brüne C, et al. (2014) Dirac-screening stabilized surface-state transport in a topological insulator. *Phys Rev X* 4:041045.
18. Kozlov DA, et al. (2014) Transport properties of a 3D topological insulator based on a strained high-mobility HgTe film. *Phys Rev Lett* 112:196801.
19. Gallagher BL, Butcher PN (1992) Handbook on Semiconductors (Elsevier Science Publishers, Amsterdam), pp 721–816.
20. Blatt J (1976) Thermoelectricity in Metallic Conductors (Springer, New York).
21. Behnia K (2015) Fundamentals of Thermoelectricity (Oxford Univ Press, Oxford).
22. Novik EG, et al. (2005) Band structure of semimagnetic $Hg_{1-y}Mn_yTe$ quantum wells. *Phys Rev B* 72:035321.
23. Baum Y, et al. (2014) Self-consistent $\mathbf{k} \cdot \mathbf{p}$ calculations for gated thin layers of three-dimensional topological insulators. *Phys Rev B* 89:245136.
24. Ivchenko EL, Kaminski AY, Rössler U (1996) Heavy-light hole mixing at zinc-blende (001) interfaces under normal incidence. *Phys Rev B* 54:5852–5859.
25. Wu S-C, Yan B, Felser C (2014) Ab initio study of topological surface states of strained HgTe. *Europhys Lett* 107:57006.
26. Liu C, et al. (2015) Tunable spin helical Dirac quasiparticles on the surface of three-dimensional HgTe. *Phys Rev B* 92:115436.
27. Xia Y, et al. (2009) Observation of a large-gap topological-insulator class with a single Dirac cone on the surface. *Nat Phys* 5:398–402.
28. Fletcher R, Harris JJ, Foxon CT, Tsaousidou M, Butcher PN (1994) Thermoelectric properties of a very-low-mobility two-dimensional electron gas. *Phys Rev B* 50:14991.
29. Slack GA, Galginaitis S (1964) Thermal conductivity and phonon scattering by magnetic impurities in CdTe. *Phys Rev* 133:A253–A268.
30. Noguera A, Wasim SM (1985) Thermal conductivity of mercury telluride. *Phys Rev B* 32:8046–8051.
31. Cantrell DG, Butcher PN (1986) A calculation of the phonon drag contribution to thermopower in two-dimensional systems. *J Phys C Solid State Phys* 19:L429–L432.
32. Behnia K (2009) The Nernst effect and the boundaries of the Fermi liquid picture. *J Phys Condens Matter* 21:113101.
33. Smrčka L, Středa P (1977) Transport coefficients in strong magnetic fields. *J Phys C Solid State Phys* 10:2153–2161.
34. Jonson M, Girvin SM (1984) Thermoelectric effect in a weakly disordered inversion layer subject to a quantizing magnetic field. *Phys Rev B* 29:1939–1946.
35. Fletcher R, Maan JC, Ploog K, Weinmann G (1986) Thermoelectric properties of GaAs $Ga_{1-x}Al_xAs$ heterojunctions at high magnetic fields. *Phys Rev B* 33:7122–7133.
36. Tieke B, Fetcher R, Zeitler U, Henini M, Maan JC (1998) Thermopower measurements of the coupling of phonons to electrons and composite fermions. *Phys Rev B* 58:2017–2025.
37. Ballet P, et al. (2014) MBE growth of strained HgTe/CdTe topological insulator structures. *J Electron Mater* 43:2955–2962.
38. Takita K, Landwehr G (1981) Very large phonon-drag thermoelectric power of HgTe in strong magnetic fields. *Phys Status Solidi B Basic Solid State Phys* 106:259–269.
39. Jedrzejczak A, Dietl T (1976) Thermomagnetic Properties of *n*-type and *p*-type HgTe. *Phys Status Solidi B Basic Solid State Phys* 76:737–751.